Graphene-loaded wire medium for tunable broadband subwavelength imaging

Ali Forouzmand,* Hossein M. Bernety, and Alexander B. Yakovlev
Department of Electrical Engineering, University of Mississippi, University, Mississippi 38677-1848, USA
(Received 12 February 2015; revised manuscript received 20 June 2015; published 3 August 2015)

In this paper, we demonstrate that a wire medium (WM) slab loaded with graphene sheets enables the enhancement of the near field for subwavelength imaging at terahertz frequencies. The analysis is based on the nonlocal homogenization model for WM with the additional boundary condition at the connection of wires to graphene. The principle of the operation of the proposed lens depends on the enhancement of evanescent waves, wherein the excited surface plasmons at the lower and upper graphene interfaces are coupled by an array of metallic wires. The resolution and the operating frequency of the subwavelength imaging device are mainly determined by the tunability of graphene and the structural parameters of the WM slab. The proposed structure has a resolution better than $\lambda/10$ with the advantages of broad bandwidth, low sensitivity to losses, and tunability with respect to the chemical potential even if the distance between two graphene sheets is a significant fraction of wavelength. Severe challenges in the fabrication of the lens have been studied in-depth, and a promising approach for a practical realization has been proposed.

DOI: 10.1103/PhysRevB.92.085402 PACS number(s): 41.20.Jb, 78.67.Wj, 42.50.St, 73.20.Mf

I. INTRODUCTION

Since the resolution of traditional optical lenses is restricted by the diffraction limit, subdiffraction imaging is of particular interest to the metamaterials community. The conventional lenses are not able to transport evanescent near-field modes that carry subwavelength information. In order to overcome this limitation, a well-known solution is to use a metamaterial lens with negative refractive index property. Veselago pointed out the possibility of the existence of a negative index material (NIM) in 1968 [1]. Following this idea, Pendry realized that a NIM slab ($\varepsilon = -1$ and $\mu = -1$) can effectively amplify the exponentially decaying evanescent modes of a source field and, thus, could focus both the evanescent and propagating spectra [2]. Pendry also noticed that a thin slab of silver with only negative permittivity would act as a near-field lens [3]. This lens, which is known as a superlens, has important applications in biomedical imaging, sensing, and nondestructive characterization of materials [4–9]. The physical mechanism behind Pendry's lens can be described as a resonant excitation of coupled surface plasmon polaritons, which are supported at the interfaces of the slab. The desired conditions for this technique can be realized at a single carefully selected frequency with high sensitivity to the absorption and frequency dispersion.

Due to the fact that Pendry's subwavelength imaging process physically arises at the lens interfaces, it is also possible to utilize a pair of resonant grids or conjugate sheets instead of a bulk material [10–13]. Graphene as a single atom layer of carbon atoms guides surface plasmons [14–16], and this phenomenon was employed for different metamaterial plasmonic applications [17–20]. Recently, Ref. [21] presented a frequency tunable graphene lens in which the enhancement of evanescent waves for subwavelength imaging is realized by the well coupled graphene sheets that can support surface plasmons. It should be noted that the structure's performance intensely depends on the distance between graphene sheets and that the subwavelength information is lost when the thickness of the lens is increased.

Another metamaterial lens with artificially engineered properties has been proposed in Refs. [22–25]. The idea is that both evanescent and propagating harmonics are transformed into the transmission-line modes along the wires in a wire medium (WM) slab. The loss sensitivity of this structure is remarkably small, and the resolution is restricted only by the spacing between the wires. It has been shown that the properties of this lens cannot be tuned after fabrication and that the thickness of WM should be chosen in such a way that it is an integer number of half wavelength to satisfy the subwavelength imaging condition.

Here, we propose a WM slab loaded with graphene sheets that provides both of the aforementioned subwavelength imaging properties of the WM and graphene. The enhancement of evanescent waves is provided by the coupling of the surface plasmons at the lower and upper interfaces. The WM slab has a remarkable effect on the strong coupling and waveguiding of evanescent waves to the other side of the structure. The modal dispersion behavior of the proposed structure can be described as the perturbation of the surface plasmons of graphene sheets by utilizing an array of metallic wires. The proposed lens has advantages of widely tunable subwavelength imaging and the possibility of obtaining an image even if the distance between two graphene sheets is a significant fraction of wavelength. In addition, the structure has a remarkable improvement in comparison to other subwavelength imaging devices in terms of bandwidth and position of a source.

The study of the transmission/reflection behavior of the graphene-dielectric stack, provided in Ref. [26], was carried out using a simple analytical transfer-matrix method (TMM). Alternatively, the analysis can be realized by using the principles of the circuit-theory model described in Ref. [27], wherein graphene sheets are modeled as shunt admittances. Also in Ref. [28], the optical properties of one-dimensional graphene-embedded quarter-wave stack have been investigated by modifying the conventional TMM [26]. Here, we deal with the analysis of the transmission/reflection properties of the WM slab loaded with graphene sheets, wherein the impinging evanescent waves excite surface plasmons at the interfaces of the structure. A nonlocal homogenization model is utilized

*sforouzm@go.olemiss.edu

[29,30] such that the WM is modeled as a uniaxial anisotropic material characterized by a nonlocal dielectric function with a generalized additional boundary condition (GABC) at the connection of wires to graphene. We employ two widely used approaches to investigate the imaging properties of the structure. First, we placed an infinite magnetic line source at a distance from the upper interface of the structure and calculated the magnetic field distribution at the same distance from the lower interface. The resolution of the lens is quantified by the Half Power Beam Width (HPBW) criterion [31]. In the second approach, the performance of the lens is assessed by a double-slit source and then interpreted by the Rayleigh criterion [32–36]. The analytical results are validated with the full-wave electromagnetic simulator, CST Microwave Studio [37], showing good agreement.

It is also worth noting that in addition to the theoretical studies described above, subwavelength imaging has been verified experimentally with different imaging structures. In Ref. [38], an experimental validation of subwavelength imaging by a WM slab has been performed at microwave frequencies. Also in Ref. [24], it has been extended to THz and infrared frequencies by employing silver nanorods. In addition to these WM lenses, recently, subwavelength imaging has been theoretically and experimentally studied in Ref. [39] by using a fishnet flat lens, wherein a three-dimensional (3D) metamaterial has been fabricated by Printed-Circuit-Board (PCB) technology. This stacked fishnet metamaterial forms waveguide channels, which provide the propagation of quasi-transverse electromagnetic (TEM) modes in the dielectric layers.

From the experimental point of view, fabrication of the graphene monolayer sheet by itself is a severe challenge. Recently, various methods have been proposed to achieve a graphene monolayer with the lowest imperfection, namely chemical vapor deposition (CVD) [40] and epitaxy [41]. The process of joining the WM to the intensely thin graphene sheet meets with some difficulties due to the fact that the well-known methods such as ohmic contact, soldering, and plasmonic welding are not applicable in the proposed structure. To overcome this limitation, here we show that a small gap between the graphene monolayer and the WM does not change the response of the lens because of the strong coupling of the surface plasmons of the graphene sheet and the WM slab. This approach has been studied by the full-wave simulation in CST Microwave Studio, which confirms this claim. In addition, the possibility of embedding the WM in a dielectric slab facilitates the fabrication and growth of the graphene sheets on the interfaces of the lens [42].

This paper is organized as follows. In Sec. II, we present the closed-form expressions for the reflection and the transmission coefficients of the WM slab loaded with graphene sheets based on the nonlocal homogenization model. The dispersion behavior of odd and even modes and the transmission response of the structure are studied in Sec. III. In Sec. IV, the performance of the proposed lens is analyzed in the presence of the magnetic line source and the double-slit source. In Sec. V, we discuss the tunability and broadband properties of the lens. The severe challenges in the practical realization of the lens have been discussed, and a promising approach to surmount these difficulties has been proposed in Sec. VI. The conclusions are drawn in Sec. VII. A time dependence of the form $e^{j\omega t}$ is assumed and suppressed.

II. NONLOCAL MODEL FOR WM WITH GRAPHENE SHEETS

Here, we consider a WM slab loaded with graphene sheets, as shown in Fig. 1(a). The WM slab consists of the metallic wires symmetrically arranged in a square lattice with the following structural parameters: a is the spacing between the wires (lattice constant), r_0 is the radius of the wires, ε_h is the dielectric permittivity of the slab, and h is the thickness of the structure. The metallic wires are oriented along the $z-$direction, and two graphene sheets are located at $z = 0$ and $z = -h$. To determine the transmission/reflection response of the structure with a transverse magnetic (TM) plane-wave excitation, the even/odd excitation mode technique is utilized. By considering the perfect electric conductor (PEC) and the perfect magnetic conductor (PMC) at the center of the wires ($z = -h/2$), the even and odd responses of the structure can be obtained. Figure 1(b) demonstrates the cross-section view in the presence of PEC/PMC symmetries.

In the nonlocal homogenization model, a WM is characterized by a uniaxial anisotropic material with the effective permittivity of $\varepsilon_{zz} = \varepsilon_h[1 - k_p^2/(k_h^2 - k_z^2)]$, where $k_h = k_0\sqrt{\varepsilon_h}$ is the wave number of the host medium, $k_0 = \omega/c$ is the free space wave number, ω is the angular frequency, c is the speed of light, k_z is the z-component of the wave vector $\vec{k} = (k_x, 0, k_z)$, and k_p is the plasma wave number as $k_p = \sqrt{(2\pi/a^2)/(\ln(a/2\pi r_0) + 0.5275)}$.

A TM-polarized plane wave excites both TEM and the extraordinary TM modes in the homogenized WM slab. First, it is assumed that the PEC plane is located at $z = -h/2$. The total magnetic fields in the air region above the structure (region 1) and in the WM slab (region 2), as shown in Fig. 1(b), can be

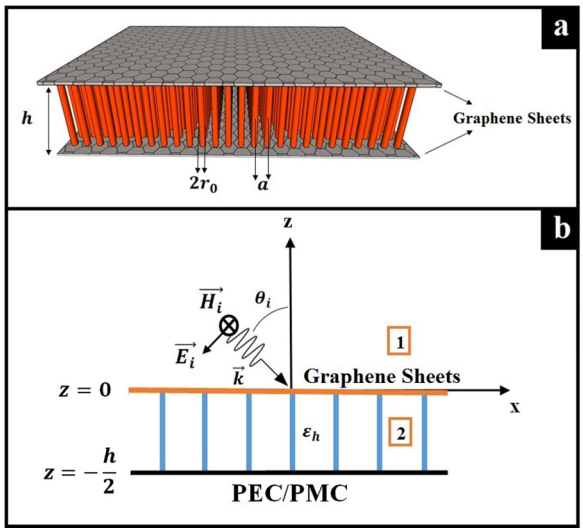

FIG. 1. (Color online) Schematics of a WM slab loaded with graphene sheets: (a) 3D view and (b) cross-section view of the structure by considering PEC/PMC at the symmetry plane.

written as follows:

$$H_y^{(1)} = (e^{\gamma_0 z} + R_{\text{even}} e^{-\gamma_0 z}) e^{-jk_x x}$$
$$H_y^{(2)} = \left(\mathrm{A}_{\text{TM}}^{+} e^{\gamma_{\text{TM}} z} + \mathrm{A}_{\text{TM}}^{-} e^{-\gamma_{\text{TM}} z} + B_{\text{TEM}}^{+} e^{\gamma_{\text{TEM}} z} + B_{\text{TEM}}^{-} e^{-\gamma_{\text{TEM}} z}\right) e^{-jk_x x}, \quad (1)$$

where $A_{\text{TM}}^{\pm}$ and $B_{\text{TEM}}^{\pm}$ are the amplitudes of the extraordinary TM and transmission-line TEM modes in the WM slab, R_{even} is the reflection coefficient of the even-mode excitation, $\gamma_0 = \sqrt{k_x^2 - k_0^2}$, $k_x = k_0 \sin\theta_i$ is the $x-$component of the wave vector $\vec{k} = (k_x, 0, k_z)$, $\gamma_{\text{TEM}} = jk_h = jk_0\sqrt{\varepsilon_h}$, and $\gamma_{\text{TM}} = \sqrt{k_p^2 + k_x^2 - k_0^2}$. In order to determine the unknown coefficients (R_{even}, $A_{\text{TM}}^{\pm}$, and $B_{\text{TEM}}^{\pm}$), the two-sided impedance boundary conditions are satisfied at the graphene interface ($z = 0$):

$$E_x^{(1)}\big|_{z=0^+} = E_x^{(2)}\big|_{z=0^-} = Z_g\left[H_y^{(2)}\big|_{z=0^-} - H_y^{(1)}\big|_{z=0^+}\right], \quad (2)$$

where the graphene sheet impedance Z_g is given by $Z_g = 1/\sigma_s$, and σ_s is graphene's complex surface conductivity ($\sigma_s = \sigma' + j\sigma''$), which is modeled with the Kubo formula using closed-form expressions for the interband (σ_{inter}) and intraband (σ_{intra}) contributions [14]:

$$\sigma_{\text{intra}} = -j\frac{k_B e^2 T}{\pi\hbar^2(\omega - j\tau^{-1})}\left(\frac{\mu_c}{Tk_B} + 2\ln\left(e^{-\frac{\mu_c}{Tk_B}} + 1\right)\right)$$
$$\sigma_{\text{inter}} \approx -\frac{je^2}{4\pi\hbar}\ln\left(\frac{2|\mu_c| - \omega\hbar}{2|\mu_c| + \omega\hbar}\right) \quad (3)$$
$$\sigma_s = \sigma_{\text{intra}} + \sigma_{\text{inter}}.$$

In Eq. (3), $\hbar$ is the reduced Planck constant, e is the electron charge, k_B is the Boltzmann's constant, T is the temperature, τ is the momentum relaxation time, and μ_c is the chemical potential. In the low-THz region and below the interband transition threshold, $\hbar\omega < 2|\mu_c|$, σ_{inter} dominates over σ_{inter} [16]. In the upper GHz and low-THz range, the imaginary part of surface conductivity has a negative value, $\sigma'' < 0$, and graphene acts as an inductive sheet [18,26]. This behavior of the surface impedance is analogous to the subwavelength metallic mesh grid at microwave frequencies. It should be noted that when $\sigma'' < 0$, a proper TM surface wave can propagate, and for $\sigma'' > 0$, a proper TE surface wave can propagate. In this paper, it is assumed that $T = 300\,\text{K}$, $\varepsilon_h = 1$, $\tau = 0.5\,\text{ps}$, $a = 215\,\text{nm}$, and $r_0 = 21.5\,\text{nm}$.

At the PEC interface ($z = -h/2$), the tangential electric field vanishes, implying that $(1/\varepsilon_h)(dH_y/dz) = 0$. Moreover, it has been shown that an additional boundary condition (ABC) is required to describe the appropriate boundary condition for the WM connected to the PEC [43–47]. The microscopic ABC, which is enforced at the PEC ground plane ($z = -h/2^+$), can be written for the wire current, $I(z)$, as [48]:

$$\left.\frac{dI(z)}{dz}\right|_{z=(-h/2)^+} = 0\,, \quad (4)$$

and in terms of macroscopic fields:

$$\left.\frac{\partial}{\partial z}\left(k_0\varepsilon_h E_z^{(2)} + k_z\eta_0 H_y^{(2)}\right)\right|_{z=(-h/2)^+} = 0. \quad (5)$$

In addition, it requires the use of GABC for the microscopic current at the connection of wires to graphene [29]:

$$\left[\frac{\sigma_s}{j\omega\varepsilon_0\varepsilon_h}\frac{dI(z)}{dz} + I(z)\right]\Bigg|_{z=0^-} = 0, \quad (6)$$

and in terms of macroscopic fields:

$$\left(1 + \frac{\sigma_s}{j\omega\varepsilon_0\varepsilon_h}\frac{\partial}{\partial z}\right)\left(k_0\varepsilon_h E_z^{(2)} + k_z\eta_0 H_y^{(2)}\right)\Big|_{z=0^-} = 0. \quad (7)$$

By enforcing the aforementioned boundary conditions, the closed-form expression of the reflection coefficient for PEC symmetry (even excitation) can be obtained by [29]

$$R_{\text{even}} = \frac{\frac{N_{\text{even}}}{D_{\text{even}}}\coth\left(\gamma_{\text{TM}}\frac{h}{2}\right)\cot\left(k_h\frac{h}{2}\right) - \left(\frac{1}{\gamma_0} + j\frac{\eta_0}{Z_g k_0}\right)}{\frac{N_{\text{even}}}{D_{\text{even}}}\coth\left(\gamma_{\text{TM}}\frac{h}{2}\right)\cot\left(k_h\frac{h}{2}\right) + \left(\frac{1}{\gamma_0} - j\frac{\eta_0}{Z_g k_0}\right)},$$
$$N_{\text{even}} = \left(\frac{1}{\varepsilon_{zz}^{\text{TM}}} - 1\right)\left(\frac{\sigma_s\gamma_{\text{TM}}}{j\omega\varepsilon_0\varepsilon_h}\tanh\left(\gamma_{\text{TM}}\frac{h}{2}\right) + 1\right) + \left(1 - \frac{\sigma_s k_h}{j\omega\varepsilon_0\varepsilon_h}\tan\left(k_h\frac{h}{2}\right)\right),$$
$$D_{\text{even}} = -\frac{k_h}{\varepsilon_h}\left(\frac{1}{\varepsilon_{zz}^{\text{TM}}} - 1\right)\left(\frac{\sigma_s\gamma_{\text{TM}}}{j\omega\varepsilon_0\varepsilon_h} + \coth\left(\gamma_{\text{TM}}\frac{h}{2}\right)\right) + \frac{\gamma_{\text{TM}}}{\varepsilon_h}\left(\cot\left(k_h\frac{h}{2}\right) - \frac{\sigma_s k_h}{j\omega\varepsilon_0\varepsilon_h}\right). \quad (8)$$

The closed-form expression of the reflection coefficient for the PMC symmetry (odd excitation) can be derived using a similar approach:

$$R_{\text{odd}} = \frac{\frac{N_{\text{odd}}}{D_{\text{odd}}}\tanh\left(\gamma_{\text{TM}}\frac{h}{2}\right)\tan\left(k_h\frac{h}{2}\right) - \left(\frac{1}{\gamma_0} + j\frac{\eta_0}{Z_g k_0}\right)}{\frac{N_{\text{odd}}}{D_{\text{odd}}}\tanh\left(\gamma_{\text{TM}}\frac{h}{2}\right)\tan\left(k_h\frac{h}{2}\right) + \left(\frac{1}{\gamma_0} - j\frac{\eta_0}{Z_g k_0}\right)},$$
$$N_{\text{odd}} = \left(\frac{1}{\varepsilon_{zz}^{\text{TM}}} - 1\right)\left(\frac{\sigma_s\gamma_{\text{TM}}}{j\omega\varepsilon_0\varepsilon_h}\coth\left(\gamma_{\text{TM}}\frac{h}{2}\right) + 1\right) + \left(1 + \frac{\sigma_s k_h}{j\omega\varepsilon_0\varepsilon_h}\cot\left(k_h\frac{h}{2}\right)\right),$$
$$D_{\text{odd}} = +\frac{k_h}{\varepsilon_h}\left(\frac{1}{\varepsilon_{zz}^{\text{TM}}} - 1\right)\left(\frac{\sigma_s\gamma_{\text{TM}}}{j\omega\varepsilon_0\varepsilon_h} + \tanh\left(\gamma_{\text{TM}}\frac{h}{2}\right)\right) + \frac{\gamma_{\text{TM}}}{\varepsilon_h}\left(\tan\left(k_h\frac{h}{2}\right) + \frac{\sigma_s k_h}{j\omega\varepsilon_0\varepsilon_h}\right), \quad (9)$$

where $\varepsilon_{zz}^{\text{TM}} = \varepsilon_h k_x^2/(k_p^2 + k_x^2)$ is the relative effective permittivity for TM polarization. The results can be validated by considering the limiting case of $\sigma_s \to 0$. In this case, (8) and (9) turn to the WM slab expressions derived in Ref. [47]. The transmission/reflection response of the structure [shown in Fig. 1(a)] can be obtained by the superposition principle as follows:

$$R = \tfrac{1}{2}(R_{\text{even}} + R_{\text{odd}})\,, \quad (10)$$
$$T = \tfrac{1}{2}(R_{\text{even}} - R_{\text{odd}}). \quad (11)$$

III. PARAMETRIC STUDY OF DISPERSION AND TRANSMISSION PROPRETIES

Here, we are interested in studying the dispersion behavior of the TM^x surface waves and the transmission response of the WM slab loaded with graphene sheets in order to determine the proper operating frequency regime in which the enhancement of evanescent waves leads to the recovering of the source details at the image plane. The ultimate goal is designing a subwavelength imaging lens with a high resolution and low distortion properties.

First, we study the dispersion relation obtained by applying the PMC plane at $z = -h/2$ [as shown in Fig. 1(b)]. The dispersion of the surface waves is calculated by finding the complex roots of the dispersion function [denominator of the reflection coefficient in Eq. (9)]. Figure 2 shows the dispersion behavior of the normalized propagation constant (k_x/k_0) of the odd TM^x modes of the WM slab loaded with graphene sheets with $\mu_c = 1.5\,\text{eV}$ and $h = 2400\,\text{nm}$. At low frequencies ($f < 18\,\text{THz}$), the real part of (k_x/k_0) is close to 1, and the imaginary part has a negligibly small negative value, indicating that the proper complex bound mode (surface plasmon) interacts weakly with the WM slab and propagates primarily in the air region in the vicinity of graphene sheet. With the increase of frequency, it interacts stronger with the structure, and at a frequency around 19.6 THz, a stopband occurs for the first TM^x surface plasmon, which corresponds to the left bound of the stopband. The cutoff frequency of the second proper complex bound mode occurs approximately at 65 THz, which is considered as the right bound of the stopband. Within the stopband for the proper bound mode (from 19.6 THz to 65 THz), a proper complex wave with $\text{Re}(k_x/k_0) > 1$ and large $\text{Im}(k_x/k_0)$ exists.

Figure 3 illustrates the dispersion behavior of the structure for the odd excitation with different thicknesses. It is observed that by increasing the length of the lens, the total behavior of the dispersion does not change drastically. However, the resonance has a remarkable shift to the lower frequencies. It leads to the expansion of the stopband regime wherein the propagation of the proper (bound) complex modes stops. For example, by changing the length from 400 nm to 3000 nm, the resonance frequency changes from 49.71 THz to 17.34 THz.

In order to provide further illustrations, Fig. 4 shows the dispersion behavior of the structure for the odd excitation with the various values of the chemical potential. The chemical potential can be largely tuned either passively, by doping the profile (density and type of carriers) or chemical/structural surface modification, or actively, by an external static electric field or magnetic field [14]. It is observed that the resonance corresponding to the left bound of the stopband occurs at lower frequencies by decreasing the graphene's chemical potential.

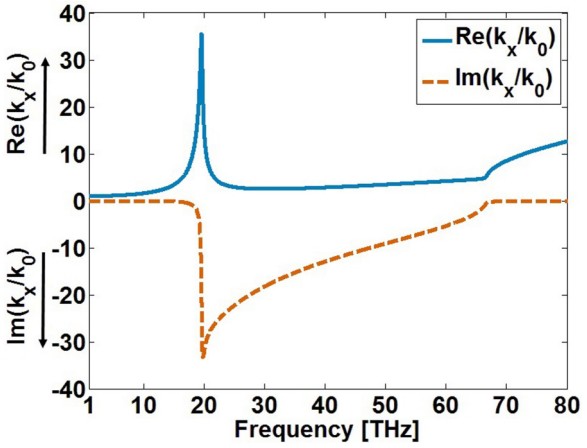

FIG. 2. (Color online) Dispersion behavior of the odd TM^x modes of a WM slab loaded with graphene sheets. The solid line represents the real part of the normalized propagation constant, $\text{Re}(k_x/k_0)$, and the dashed line represents the imaginary part of the normalized propagation constant, $\text{Im}(k_x/k_0)$.

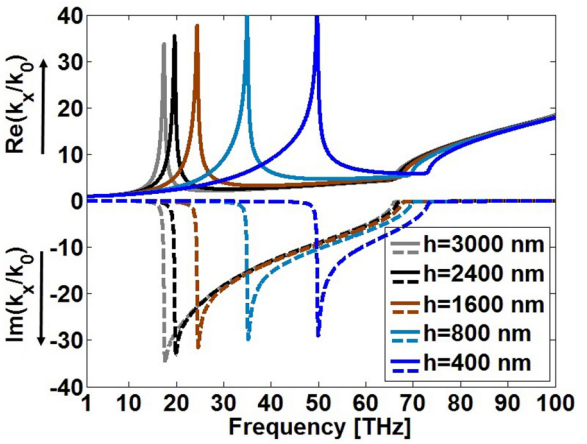

FIG. 3. (Color online) Dispersion behavior of the odd TM^x modes of the WM slab loaded with graphene sheets with different structure's thicknesses in the range from 400 to 3000 nm. The solid line represents the real part of the normalized propagation constant, $\text{Re}(k_x/k_0)$, and the dashed line represents the imaginary part of the normalized propagation constant, $\text{Im}(k_x/k_0)$.

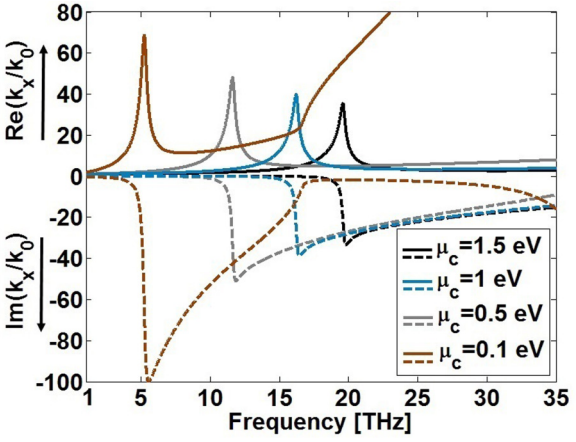

FIG. 4. (Color online) Dispersion behavior of the odd TM^x modes of the WM slab loaded with graphene sheets with different chemical potentials in the range from 0.1 to 1.5 eV. The solid line represents the real part of the normalized propagation constant, $\text{Re}(k_x/k_0)$, and the dashed line represents the imaginary part of the normalized propagation constant, $\text{Im}(k_x/k_0)$.

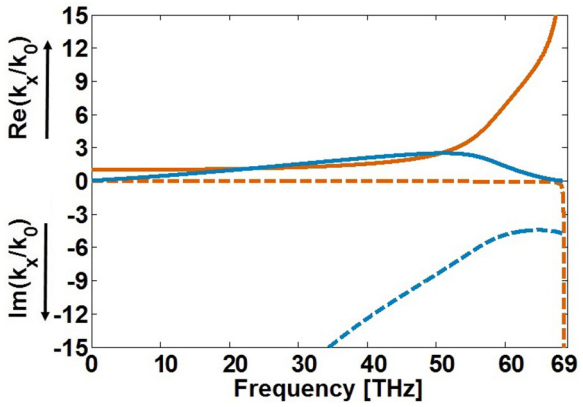

FIG. 5. (Color online) Dispersion behavior of the even TM^x modes of the WM slab loaded with graphene sheets. The solid line represents the real part of the normalized propagation constant, Re(k_x/k_0), and the dashed line represents the imaginary part of the normalized propagation constant, Im(k_x/k_0).

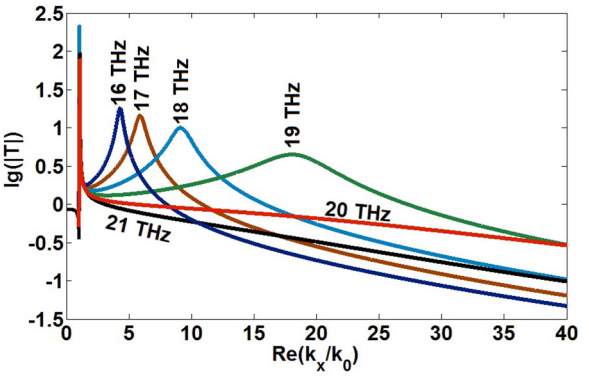

FIG. 6. (Color online) Magnitude of the transmission coefficient as a function of k_x/k_0 calculated for a WM slab loaded with graphene sheets in the range from 16 to 21 THz.

The length of the structure is set to $h = 2400$ nm for all of the cases.

Similarly, the response of the structure for the even excitation can be obtained by applying the PEC symmetry in Fig. 1(b). In this regard, Fig. 5 shows the dispersion behavior of the normalized propagation constant (k_x/k_0) of the even TM^x modes of the WM slab loaded with graphene sheets with $\mu_c = 1.5$ eV and $h = 2400$ nm. When the real part of (k_x/k_0) is close to 1 and the imaginary part has a small negative value, it indicates that the proper complex (bound) mode interacts weakly with the structure and propagates in the air region in the vicinity of graphene sheets (the solid/dashed brown lines at the frequencies below 50 THz). The other mode as an improper complex leaky wave (solid/dashed blue lines) has a similar dispersion behavior for Re(k_x/k_0) for the frequencies up to 50 THz. Since Im(k_x/k_0) of this mode has a large value, the wave attenuates and does not radiate. In this paper, we are interested in subwavelength imaging at low THz frequencies. Therefore, the dispersion behavior at high THz frequencies (frequencies higher than 50 THz) has not been discussed in details. By a careful study of the dispersion relation for odd and even excitations, it concludes that the significant resonance of the structure is associated with the odd modes at low-THz frequencies, and thus, we restrict our analysis to the modes obtained with the PMC symmetry. However, at frequencies higher than 50 THz, the dispersion behavior of the TM^x surface waves for the even excitation, shown by the black line in Fig. 5, keeps increasing, unlike other modes, and the imaginary part has a small negative value. Therefore, it should be mentioned that both even and odd excitations play important roles in the formation of resonances with a higher value of k_x/k_0 in this frequency range.

The other criterion that can provide more quantitative and detailed information about the structure's performance in subwavelength imaging is the transmission response of the device as a function of wave vector k_x/k_0 [49]. The behavior of the transmission coefficients is sensitive to the variations in the operating frequency. Therefore, the transmission magnitude $|T|$ as a function of Re(k_x/k_0) is calculated at different frequencies of operation in the range from 16 to 21 THz and is depicted in Fig. 6. It is shown that the reduction of the frequency of operation reveals a significant resonant phenomenon, which leads to the enhancement of the amplitude of the evanescent modes for a certain range of k_x. The observed resonant enhancement deteriorates the subwavelength imaging since some of the spatial harmonics are amplified by a large factor. In contrast, for the frequencies close to 19 THz, the resonant behavior has not been observed in the transmission coefficients, and the transmission magnitude is close to unity for a larger range of spatial harmonics.

We study in detail the dispersion behavior and the transmission response considered as two important parameters in the formation of the subwavelength imaging. As shown in Figs. 2 and 6, at frequencies lower than 18 THz, the imaginary part of the normalized propagation constant of the proper bound mode has a small value [Im(k_x/k_0) ≈ 0], and thus, the transmission intensity will be large at the resonance that leads to the overamplification of some of the Fourier components (k_x). This phenomenon diverges the transmission and deteriorates the subwavelength imaging. For this reason, the subwavelength imaging is not possible in this region. In addition, the real part of the normalized propagation constant (Re(k_x/k_0)) is nearly equal to 1, which leads to a transmission resonance at the vicinity of Re(k_x/k_0) = 1. At 18 THz $< f <$ 19.6 THz, the imaginary part of the propagation constant increases and prevents the divergence of the transmission and effectively moderates the effects of the resonance. It should be mentioned that although the imaginary part of (k_x/k_0) by itself would not cause a fundamental improvement in the image resolution, any finite amount of Im(k_x/k_0) in the slab will not allow the transmission to diverge. In this region, by increasing the frequency the resonance peak shifts to a greater value of Re(k_x/k_0) of the proper complex bound mode, which means that a larger number of Fourier components can be transferred with a transmission coefficient equal or slightly greater than 1, leading to a better resolution for the structure. At 19.6 THz $< f <$ 22 THz, the subwavelength imaging is obtained by weak coupling of evanescent waves from the source to the proper complex wave with both large values of Re(k_x/k_0) and Im(k_x/k_0), which exists in the stopband region for the proper complex bound waves. At frequencies higher

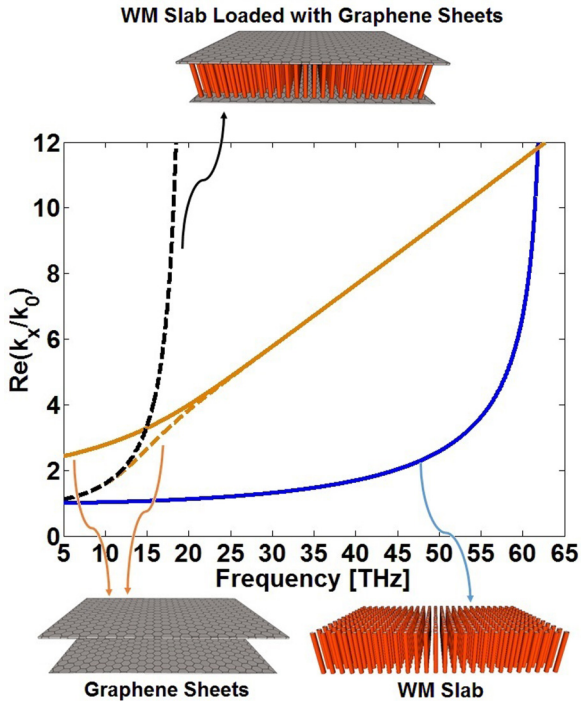

FIG. 7. (Color online) Dispersion behavior of the WM slab loaded with graphene sheets (black line), the isolated WM slab (blue line), and two parallel graphene sheets (orange line). The solid lines represent the real part of the normalized propagation constant for even excitation (PEC symmetry), and the dashed lines represent the real part of the normalized propagation constant for odd excitation (PMC symmetry).

than 22 THz, the transmission coefficient decays drastically because of the large value of $\mathrm{Im}(k_x/k_0)$ and the small value of $\mathrm{Re}(k_x/k_0)$ of the proper complex wave; as a result, the structure has a poor performance in terms of subwavelength imaging. By a careful study of the dispersion relation and the transmission coefficient, it can be concluded that the proper frequency regime is $18.5 - 22$ THz for the aforementioned parameters. In Sec. IV, we investigate the validity of this claim.

In order to provide more clarifications regarding the distinct properties of the WM slab loaded with graphene sheets in comparison with the isolated WM slab and parallel graphene sheets, Fig. 7 shows the dispersion behavior of the bound modes for these three cases with the following parameters: $a = 215$ nm, $r_0 = 21.5$ nm, $\mu_c = 1.5$ eV, and $h = 2400$ nm. The blue solid line represents $\mathrm{Re}(k_x/k_0)$ for the even excitation of the isolated WM slab. At frequencies around 62.5 THz corresponding to $h = \lambda/2$, a stopband occurs for the first TM^x surface-wave mode. It is observed that the second stopband can be obtained by utilizing the odd excitation at $f = 125$ THz ($h = \lambda$). This phenomenon arises due to the fact that the WM slab acts as a Fabry-Pérot resonator at frequencies in which the thickness of the structure is an integer number of half wavelength ($h = n\lambda/2, n = 1, 2, 3, \ldots$). The solid and dashed orange lines present the dispersion behavior of the two parallel graphene sheets for the even and odd excitations, respectively. It can be clearly seen that the dispersion behavior of the WM slab loaded with graphene sheets is remarkably different from the isolated WM slab and the two parallel graphene sheets. Figure 7 conveys two important points. First, at low frequencies, the modal behavior of the proposed structure can be described as a perturbation of the surface plasmons of two parallel graphene sheets, and it is similar to the dispersion of bound modes in the WM slab at higher frequencies, resulting in a Fabry-Pérotstopband. The graphene sheets and the WM slab can modulate each other's surface plasmons when they are placed in ultimate close vicinity of each other. Second, the resonance behavior of the proposed structure can be explained in terms of the Fabry-Pérot resonance when the electrical thickness of the slab is larger than its physical thickness ($h = 2400$ nm) [27,50,51]. It is worth noting that the intrinsically inductive property of graphene at low-THz frequencies provides the required excess length to satisfy the Fabry-Pérot resonance condition.

Figures 8(a) and 8(b) represent the magnitude and phase of the magnetic field distribution along the z-axis for the WM slab loaded with graphene sheets with the following structural parameters: $a = 215$ nm, $h = 2400$ nm, $\mu_c = 1.5$ eV, and $r_0 = 21.5$ nm at the operating frequency of $f = 19.6$ THz (this frequency corresponds to the maximally flat dispersion response of the lens as shown in Fig. 2). Figure 8(a) demonstrates that the distribution of magnetic field inside the WM slab loaded with graphene sheets is analogous to the shape of a Fabry-Pérot standing wave. However, its behavior is different in the vicinity of graphene sheets due to the strong coupling to the surface plasmons at the interfaces of the lens. Although the ideal Fabry-Pérot resonance will result in the phase shift of π for the incident magnetic field in the WM slab with the thickness of $\lambda/2$ [52], Fig. 8(b) shows the phase shift of 154° along the wires for WM slab loaded with graphene sheets. This difference with the ideal Fabry-Pérot resonance is attributed due to the loss effect of graphene sheets, which leads to a finite value of wave number k_x/k_0 at the resonance frequency. In contrast, operating at the frequency of flat dispersion in the lossless WM slab will result in canalization of all spatial

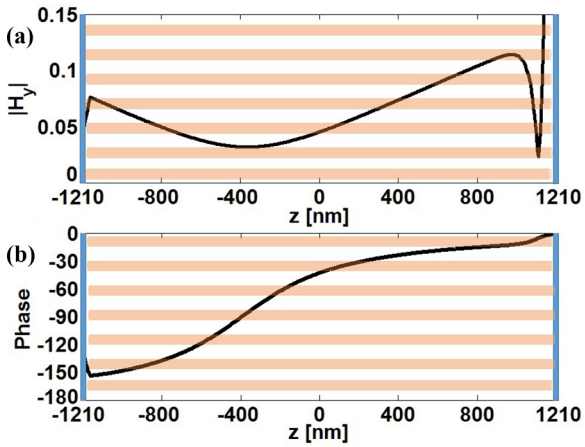

FIG. 8. (Color online) (a) Magnitude (unit: A/m) and (b) phase of the magnetic field distribution along the z direction for a WM slab loaded with graphene sheets excited by the magnetic line source located at $z = 1350$ nm. The vertical blue bars show the position of the graphene sheets, and the horizontal red bars show the WM slab.

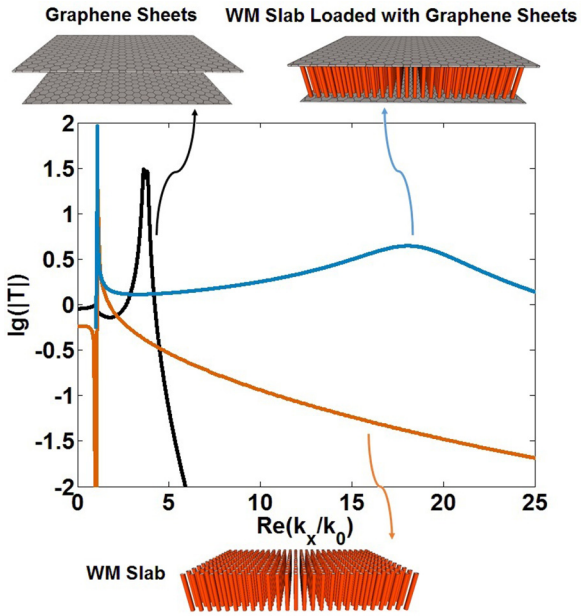

FIG. 9. (Color online) Magnitude of the transmission coefficient as a function of k_x/k_0 calculated for a WM slab loaded with graphene sheets, isolated WM slab, and two parallel graphene sheets.

harmonics (k_x) along the wires with the same phase velocity (the same wave number k_z).

In Fig. 9, we show the transmission characteristics of the WM slab loaded with graphene sheets, the isolated WM slab, and two parallel graphene sheets at the operating frequency of $f = 19$ THz. Due to the fact that the structure thickness is not an integer number of the half wavelength ($h = \lambda/6.58$), the transmission magnitude of the WM slab is lower than 1 ($\lg(|T|) = 0$) and decays rapidly. The transmission of two graphene sheets has two resonances at $k_x/k_0 = 3.623$ and 3.816, then it drops drastically. Figure 7 shows that the first resonance corresponds to the odd excitation (dashed orange line), and the second resonance is related to the even excitation (solid orange line) [21]. Rather differently, the transmission curve is smooth and close to unity ($\lg(|T|) = 0$) for a large range of k_x in our proposed structure, which means that two graphene sheets are strongly coupled (even if the thickness of the slab is a large fraction of wavelength) and the near field can be effectively transferred by the array of metallic wires. The physical mechanism of our proposed structure can be explained as the resonant excitation of the surface waves supported by the graphene sheets assisted by the canalization effect of the WM slab.

IV. STUDY OF RESOLUTION

In order to evaluate the subwavelength imaging resolution of a structure, various techniques have been proposed. Here, we utilize two well-known methods to characterize the imaging properties of the structure. The performance of the lens is studied in the presence of the magnetic line and double-slit sources, and the resolution is evaluated by using the HPBW and the Rayleigh criteria.

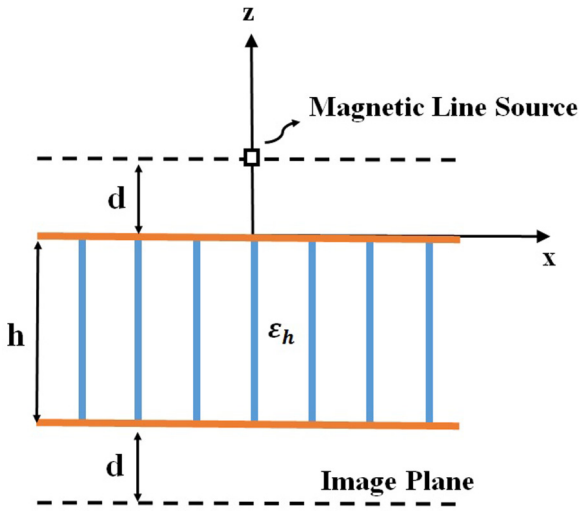

FIG. 10. (Color online) Geometry of the WM slab loaded with graphene sheets excited by a magnetic line source placed at a distance d from the upper interface, with the image plane at a distance d from the lower interface.

A. Magnetic line source

We consider an infinite magnetic line source oriented along the $y-$ direction and placed it at a distance d from the upper interface of the structure. The geometry is shown in Fig. 10. The current density of the infinite magnetic line source is $\boldsymbol{J}_m = I_0\delta(z-d)\delta(x)\hat{\mathbf{y}}$, with the excited magnetic field given by

$$\boldsymbol{H}(x,z) = \frac{I_0 k_0^2}{j\omega\mu_0}\left[\frac{1}{4j}H_0^{(2)}(k_0\rho)\right]\hat{\mathbf{y}}\,, \tag{12}$$

where $\rho = \sqrt{x^2+(z-d)^2}$ and $H_0^{(2)}(k_0\rho)$ are the zero order Hankel function of the second kind. The magnetic field at a distance d from the lower interface of the structure can be obtained by a Sommerfeld-type integral as [31]:

$$H_y(x) = \frac{I_0 k_0^2}{j\pi\omega\mu_0}\int_0^\infty \frac{1}{2\gamma_0}e^{-\gamma_0(2d)}T(\omega,k_x)\cos(k_x x)dk_x, \tag{13}$$

where $\gamma_0 = \sqrt{k_x^2 - k_0^2}$ is the propagation constant in free space and $T(\omega,k_x)$ is the transfer function of the structure defined in Eq. (11).

Figure 11 shows the square normalized amplitude of the magnetic field profile calculated at the image plane as a function of x/λ at the operating frequency of $f = 19$ THz. It is assumed that the magnetic line source is located at $d = 150$ nm. The blue solid line has been obtained by the numerical integration of the Sommerfeld integral in Eq. (13). According to the HPBW criterion, the resolution is approximately 0.1λ. The dashed line represents the performance of the proposed lens studied by using the electromagnetic simulator CST Microwave Studio, and the same resolution is obtained (0.1λ). The black solid line represents the magnetic field profile for the propagation in free space with the resolution of 0.65λ. The resolution of the proposed structure is approximately 6.5 times better than the resolution in free space. The resolution of $\lambda/10$ for the structure has been obtained analytically

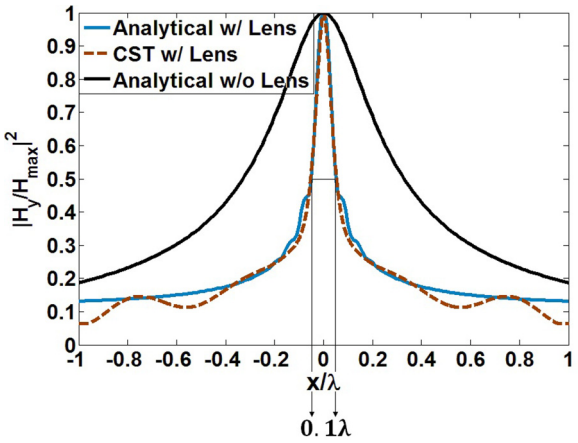

FIG. 11. (Color online) The square normalized amplitude of the magnetic field H_y calculated at the image plane for $f = 19$ THz. The black curve represents the field profile when the structure is absent. The blue curve is the field profile in the presence of the structure, and the dashed line corresponds to the CST Microwave Studio result.

and verified with the full-wave simulation. At $f = 19$ THz, as shown in Fig. 6, the enhanced transmission curve is relatively smooth and flat in the range before approaching the first peak ($k_x < 10\,k_0$), which means that the structure transfers the evanescent fields in this range without distortion. The amplitude of the transmission exceeds 1 [$\lg(|T|) = 0$] at the resonance ($k_x = 18\,k_0$) and causes the enhancement of the decaying evanescent wave components. This amplification is helpful in compensating the decaying effect of the air gaps above and below the structure ($2d = 300$ nm).

In the CST Microwave Studio, the magnetic line source is modeled by a current-carrying square loop, and the structure is assumed periodic along the y direction; the width of the slab has been fixed at $2.22\lambda_0$ along the x direction. The metallic wires are modeled as the copper metals ($\sigma = 5.8 \times 10^7$ S/m), and the effect of ohmic losses is taken into account. A snapshot of the magnetic field (H_y) in the $x - z$ plane calculated using CST is shown in Fig. 12 at $f = 19$ THz. The image can be observed at the lower interface of the structure. The resolution

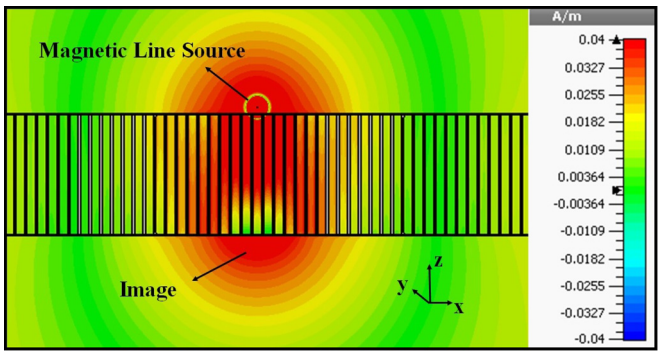

FIG. 12. (Color online) CST simulation result for the magnetic field distribution H_y of a WM slab loaded with graphene sheets. The magnetic line source is located at a distance of $d = 150$ nm from the upper interface of the structure, and the image plane is located at the same distance from the lower interface.

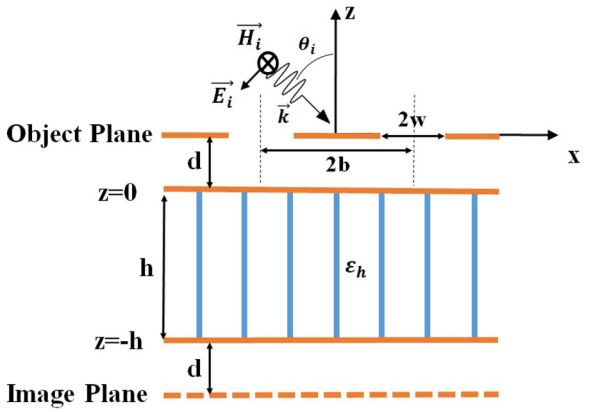

FIG. 13. (Color online) Geometry of the WM slab loaded with graphene sheets excited by a double-slit source placed at a distance d from the upper interface, with the image plane at a distance d from the lower interface.

of the image is $\lambda/10$, and it is nearly insensitive to the effect of losses.

B. Double-slit source

To obtain a rough estimate of the resolution of the proposed structure, we utilize the double-slit source at a distance d from the upper interface of the structure, as shown in Fig. 13. The double-slit source consists of two subwavelength slits ($2w$) spaced at a distance of $2b$ apart (center to center). As a starting point, we consider a TM-polarized electromagnetic wave, with H_y, E_x, and E_z components, impinging on the structure. The incident electric field $E_i(k_x)$ and the transmitted electric field $E_t(k_x)$ can be written as [35]

$$\boldsymbol{E}_i(k_x) = e^{-jk_x x + jk_z z}(-k_x\hat{\boldsymbol{z}} - k_z\hat{\boldsymbol{x}}) \tag{14}$$

$$\boldsymbol{E}_t(k_x) = T e^{-jk_x x} e^{+jk_z(z+h)}(-k_x\hat{\boldsymbol{z}} - k_z\hat{\boldsymbol{x}}), \tag{15}$$

where T is the transmission function of the WM slab loaded with graphene sheets, which is obtained in Sec. II. The electric field of the double-slit source (E_s) can be calculated by [35]

$$\boldsymbol{E}_s = \int_0^\infty dk_x\, v_{k_x} e^{jk_z z}\left(-\hat{z}\cos(k_x x) + \hat{x}\,\frac{jk_z}{k_x}\sin(k_x x)\right), \tag{16}$$

where $v_{k_x} = (\frac{4}{\pi k_x})\sin(k_x w)\cos(k_x b)$ is the Fourier component of the aperture. The distribution of the transmitted near field at the image plane can be obtained by the integration of Eq. (15) with $\frac{v_{k_x}}{k_x}$ over k_x.

To verify the subwavelength resolution, we study the electric field distribution by means of two narrow slits with $2w = 1000$ nm separated by the distance of $2b = 1500$ nm ($\lambda/10$ for the central operating frequency $f = 20$ THz). Figure 14 depicts the normalized electric field intensity distribution calculated at the image plane ($d = 150$ nm) for $f = 18.5$ THz (the lowest proper operating frequency). The black solid line represents the normalized intensity of the electric field for propagation in free space. It is observed that in the absence of the proposed structure, the subwavelength information is lost rapidly with the distance from the source

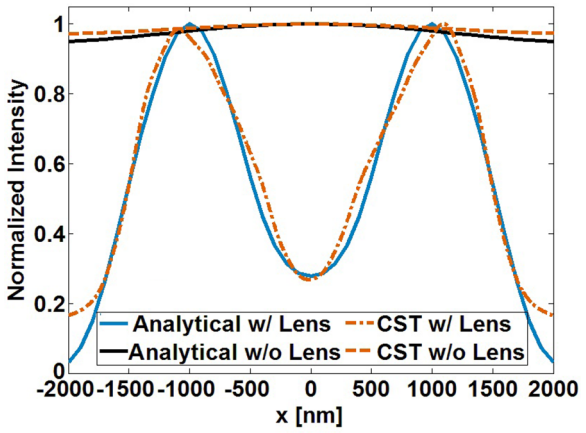

FIG. 14. (Color online) The normalized electric field intensity distribution calculated at the image plane for $f = 18.5$ THz. The black curve represents the field profile when the structure is absent. The blue curve is the field profile in the presence of the structure, and the dashed and dash-dotted lines correspond to the CST Microwave Studio results.

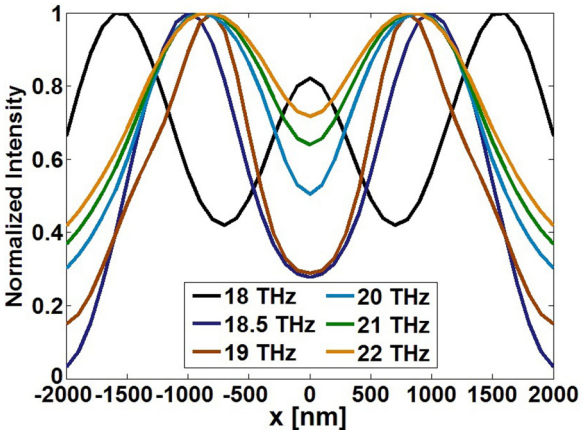

FIG. 15. (Color online) The normalized electric field distribution calculated at the image plane for a WM slab loaded with graphene sheets in the range from 18 to 22 THz.

plane, and the two slits are not resolvable. The field intensity profile at the image plane is depicted by the blue solid line when the structure is present. In the presence of the structure, the image is completely resolved according to the Rayleigh criterion, which states that the total intensity at the midpoint of the sum intensity profile of two just-resolved slit sources is 81% of the maximum intensity [53]. We compare the analytical results with the numerical results using CST Microwave Studio. In Fig. 14, the dashed and dash-dotted lines represent the imaging performance with and without the proposed lens, which are obtained with CST Microwave Studio. It can be clearly seen that there is remarkable agreement between analytical and simulation results.

Unlike other subwavelength imaging devices that have the common restriction of narrow spectral bandwidth and the increase/decrease of the incident wave frequency results in the complete loss of the resolution in the image plane, it is possible to obtain subwavelength imaging in a broad frequency range with no change in the parameters of the structure. In Fig. 15, we provide the normalized electric field intensity distribution profiles at the image plane in the frequency range from 18 to 22 THz. It is apparent that the resolution of the structure becomes degraded with increasing the frequency. It is worth noting that even in the worst case ($f = 22$ THz), two subwavelength slits can be resolved according to the Rayleigh criterion. Therefore, the proposed structure can cover a wide range of frequencies even if the parameters of the structure are kept the same. Figure 15 reveals two important points. First, the position of the maximum intensity is not matched with the position of the slit source center (the shift value is smaller than 1/6 of the slits separation). This shift effect arises from the imperfect property of the transmission function. As shown in Fig. 9, the transmission magnitude ($|T|$) does not behave uniformly and exceeds unity, especially for the frequencies lower than 19 THz, and thus the near field evanescent waves are effectively restored but in a manner of overamplification. This phenomenon would result in the destructive effects for the image profile of a double-slit source such as the large side lobes, the fat profile of the main lobe, and the significant shift of the intensity peak position. Second, as shown in Fig. 15, an extra bump appears between the two maxima of the intensity profile for $f = 18$ THz. The bump also arises from the imperfect transmission of the evanescent waves with a huge overamplification at the resonance, as shown in Fig. 6. Fortunately, the level of the bump and the shift of maxima as the artifacts of imaging are not significant enough to cause a considerable effect on resolving the two slits at the frequency range $f = 18.5$ to 22 THz.

The total electric field distribution of the WM slab loaded with graphene sheets, the isolated WM slab, and two parallel graphene sheets with the following parameters $a = 215$ nm, $r_0 = 21.5$ nm, $h = 2400$ nm, and $\mu_c = 1.5$ eV, are calculated in the $x - z$ plane by using CST Microwave Studio and are shown in Fig. 16. Figure 16 shows a plane wave with $f = 19$ THz, which is incident on the double-slit source from the left. Figures 16(a) and 16(b) represent the field distributions in the presence of two graphene sheets and the isolated WM slab, respectively. In these cases, all subwavelength information is lost at a short distance away from the slits. The near fields decay rapidly, and the two subwavelength slits are not resolved at the position of the image plane. On the other hand, Fig. 16(c) illustrates that the WM slab loaded with graphene sheets can effectively transmit the near field information of the source to the image plane, and the two subwavelength slits are clearly resolved. The results are consistent with the transmission behaviors of the aforementioned cases in Fig. 9.

V. TUNABLE AND BROADBAND SUBWAVELENGH IMAGING

In this section, we present a possibility of tuning the imaging frequencies of the WM slab loaded with graphene sheets by changing the chemical potential of graphene. As shown in Fig. 4, the structure's performance depends intensely on the chemical potential of graphene. It is observed that by decreasing the chemical potential, the appropriate operating frequency range, which leads to a high resolution subwavelength imaging, will decrease. For instance, if we

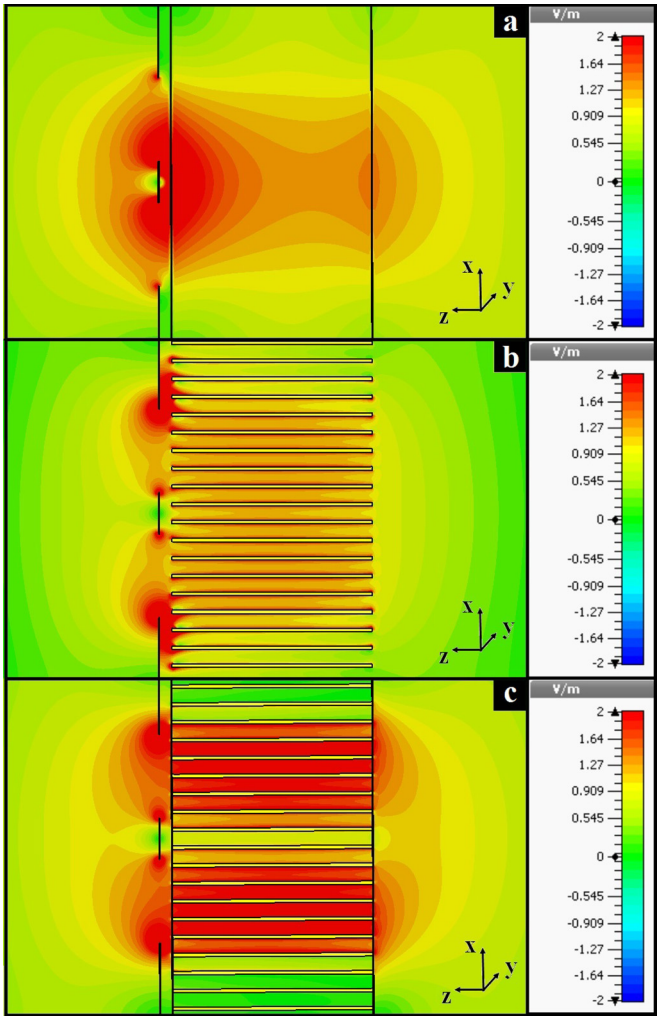

FIG. 16. (Color online) CST simulation results for the electric field distribution of (a) two graphene sheets, wherein all subwavelength information is lost and two slits are not resolvable; (b) a WM slab, showing that the subwavelength information is not transmitted to the image plane; and (c) a WM slab loaded with graphene sheets that restores the field distribution from the object plane. The double-slit source is located at a distance of $d = 150\,\text{nm}$ from the upper interface of the structure. Two slits are separated by a distance of $2b = 1500\,\text{nm}$, and the width of the slits is $2w = 1000\,\text{nm}$.

change the chemical potential from 1.5 eV to 0.5 eV, the operating frequency range decreases from $(18.5 - 22)$ THz to $(10.5 - 13)$ THz.

Here, we investigate a structure with the same parameters as in the previous section except that the graphene's chemical potential is changed from 1.5 eV to 0.5 eV. Figure 17 shows the square normalized amplitude of the magnetic field profile calculated at the image plane as a function of x/λ at the operating frequency of 11 THz. We consider $d = 150\,\text{nm}$, and the magnetic line source is placed at $z = 150\,\text{nm}$. The blue solid line is obtained by the analytical technique at the image plane. The resolution based on the HPBW criterion is 0.065λ. The dashed line shows the full wave simulation result achieved by using CST Microwave Studio, and the HPBW resolution is equal to 0.088λ. The black solid line

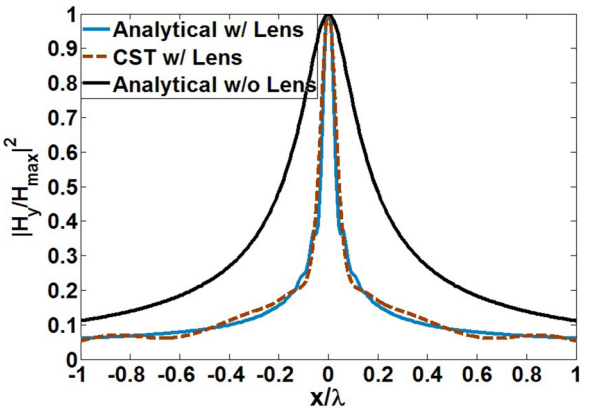

FIG. 17. (Color online) The square normalized amplitude of the magnetic field H_y calculated at the image plane for $f = 11\,\text{THz}$. The black curve represents the field profile when the structure is absent. The blue curve is the field profile in the presence of the structure, and the dashed line corresponds to the CST Microwave Studio result.

corresponds to the magnetic field propagation in free space with the resolution of 0.38λ. The resolution of the proposed structure improves nearly 5.85 times in comparison to free space. According to HPBW criterion, the resolution of $\lambda/15$ has been obtained analytically and validated by the full-wave simulation. As an important point, it should be mentioned that the better performance of the lens in terms of the resolution in comparison with the case of $\mu_c = 1.5\,\text{eV}$ occurs because the dispersion curve of the structure has a larger value of $\text{Re}(k_x/k_0)$ at the resonance frequency, which leads to the higher and more uniform transmission response. A snapshot of the magnetic field distribution in the $x - z$ plane calculated using CST Microwave Studio is shown in Fig. 18 at $f = 11\,\text{THz}$. The magnetic line source is placed at a distance of $d = 150\,\text{nm}$ from the upper structure's interface, and the image plane is at the same distance from the lower interface.

It has been shown in Sec. III that the strong enhancement of the evanescent waves ideally can be obtained when the dispersion response of the structure becomes maximally flat at the operating frequency. The physical mechanism behind this condition can be described as the efficient coupling of evanescent waves with larger wave vectors to the

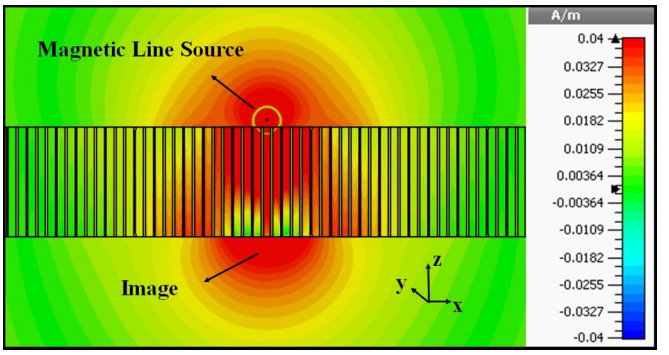

FIG. 18. (Color online) CST simulation result for the magnetic field distribution H_y of a WM slab loaded with graphene sheets at operating frequency $f = 11\,\text{THz}$ and chemical potential of $\mu_c = 0.5\,\text{eV}$.

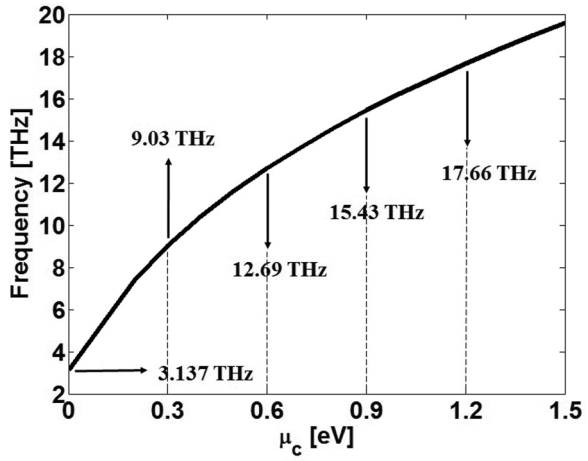

FIG. 19. The best operating frequency for subwavelength imaging versus chemical potential of graphene.

surface-wave modes, which causes the resonant interaction. Figure 19 represents the best operating frequency, which corresponds to the flat dispersion relation as a function of the chemical potential.

In addition to the tunability, we investigate the possibility of obtaining subwavelength imaging in a broad frequency range for the proposed structure with $\mu_c = 0.5$ eV and $h = 2400$ nm. In Fig. 20, the magnetic line source is placed at $d = 150$ nm, and the magnetic field profiles are calculated at the image plane in the frequency range from 10.5 to 13 THz. It can be seen that the resolution based on the HPBW criterion is better than $\lambda/7$ in this frequency range. Therefore, the proposed structure can cover a wide range of frequencies with fixed structural parameters.

The proposed structure has a remarkable improvement in comparison to other subwavelength imaging devices such as stacked graphene monolayers, wherein the source and object are positioned in the immediate vicinity of the lens [21] and the WM slab, where the source and image planes are located at a distance $d = a/2$ from the WM [22–25]. It is observed

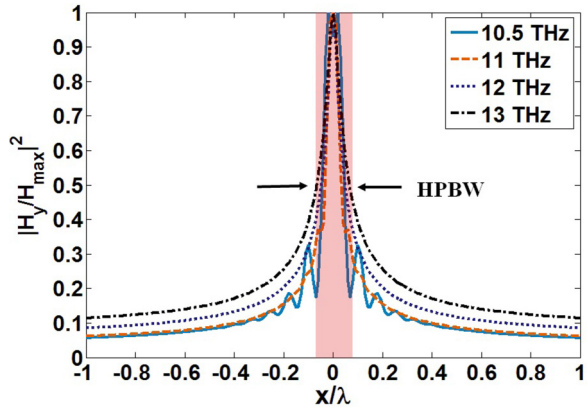

FIG. 20. (Color online) Subwavelength imaging performance of a WM slab loaded with graphene sheets ($\mu_c = 0.5$ eV) at different frequencies. The square normalized amplitude of the magnetic field H_y calculated at the image plane located at $d = 150$ nm from the structure in the range from 10.5 to 13 THz.

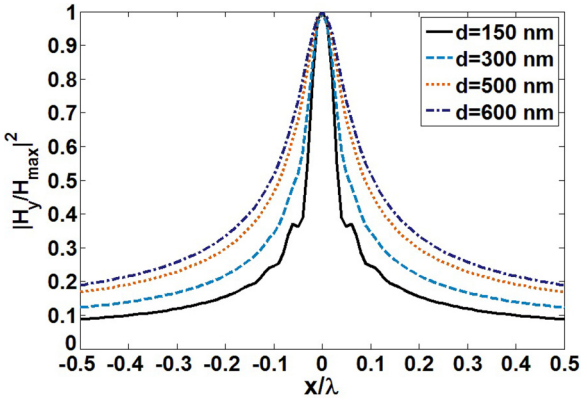

FIG. 21. (Color online) Subwavelength imaging performance of a WM slab loaded with graphene sheets ($\mu_c = 0.5$ eV) at different distances of the source and image planes from the structure.

that our lens can provide subwavelength imaging even when the source and object planes are placed at distances larger than the lattice constant of the WM slab. For example, here we assume a WM slab loaded with graphene sheets with $\mu_c = 0.5$ eV and $h = 2400$ nm at the operating frequency of $f = 11$ THz. The image/source plane has been considered to be at different distances in the range from $d = 150$ nm to $d = 600$ nm. It should be mentioned that although the distance is increased significantly in comparison to the lattice constant, the resolution of $\lambda/5$ is obtained for $d = 600$ nm ($d = 2.79a$), as shown in Fig. 21. In order to obtain a better resolution with the same structure, a stronger amplification of the near field to compensate the exponentially decaying effect of the air gaps is necessary. This phenomenon can be realized by reducing the frequency. For example, if the magnetic line source is placed at $d = 500$ nm ($d = 2.32a$), the magnetic field profile at the image plane shows the resolution of $\lambda/6.66$ at the operating frequency $f = 10$ THz, which is improved in comparison to the resolution of $\lambda/5.55$ at $f = 11$ THz. This result is omitted here for the sake of brevity.

VI. FABRICATION GUIDE

The investigation on growing of graphene has been a controversial subject for researchers since its discovery in 2003. Two of the recently proposed methods are CVD [40] and epitaxy [41]. As mentioned in Ref. [40], the CVD is more desirable from the fabrication point of view, wherein the graphene is grown on a nickel substrate, and then it can be transferred to a silicon-dioxide (SiO_2) substrate. It is worth noting that this transfer process can be applied to any arbitrary substrate (Fig. 1 in Ref. [42]), and the material properties of the graphene will be maintained and depend only on the initial nickel substrate.

It should be emphasized that throughout this paper we have assumed an ideal contact between the graphene and the WM. Additionally, we have assumed that the wires are of identical length. In fact, these two assumptions face challenges when it comes to a fabrication process. Recently, the joining of nanowires has become a critical issue for device integration and miniaturization [54]. Various joining processes such as welding and soldering have been developed for the formation

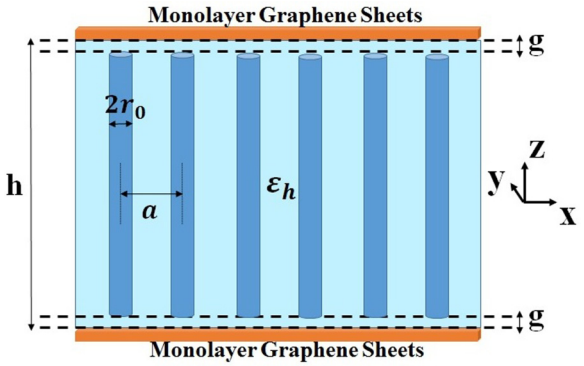

FIG. 22. (Color online) Schematics of a WM slab embedded in a dielectric slab with the permittivity of ε_h loaded with graphene sheets, which are placed at a distance of g (gap size) on the upper and lower interfaces of the structure.

of the nanowire contacts. However, up to now, it has not been possible to solder or weld a nanowire to a graphene monolayer. In addition, the well-known plasmonic welding only concerns joining two similar plasmonic materials, which is not applicable here.

To avoid the problem with connecting the wires to graphene and a nonuniform wire growth that may occur in the fabrication process, we consider a gap between the wires and the graphene sheets, as depicted in Fig. 22. As an example, we consider a WM slab loaded with graphene sheets with the following parameters: $a = 215\,\text{nm}$, $r_0 = 21.5\,\text{nm}$, $\mu_c = 1.5\,\text{eV}$, $\varepsilon_h = 1$, and $h = 2400\,\text{nm}$. Figure 23 shows the normalized amplitude of the magnetic field profile calculated at the image plane as a function of x/λ at the operating frequency of $f = 19\,\text{THz}$ for different values of the gap ($g = 0$, 10, 15, and 25 nm). The magnetic line source is located at $d = 150\,\text{nm}$ from the upper side of the structure. The solid blue line represents the performance of the structure for an ideal contact between the nanowires and the graphene sheets, and the resolution of the structure is $\lambda/10$. By increasing the gap up to 10 nm, the strong coupling between the surface plasmons of the graphene sheets and the WM leads to a subwavelength imaging with high resolution and low distortion, as shown in Fig. 23. The response

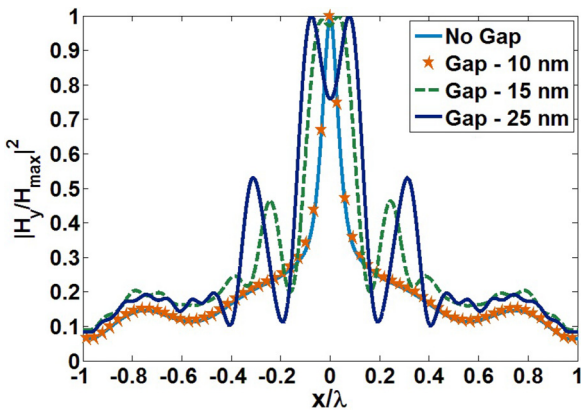

FIG. 23. (Color online) The square normalized amplitude of the magnetic field (H_y) calculated at the image plane located at $d = 150\,\text{nm}$ from the structure at the operating frequency of $f = 19\,\text{THz}$ for different values of gap ($g = 0$, 10, 15, and 25 nm).

of the structure for $g = 10\,\text{nm}$ is shown by the brown star symbols. Further increase in the gap size causes a significant distortion in subwavelength imaging, wherein remarkable side lobes appear in the magnetic field distribution at the image plane. This phenomenon arises due to strongly confined surface plasmons on graphene sheets, which consequently avoid the strong coupling between the surface plasmons of graphene and the WM slab for larger gaps.

In addition, in order to clarify qualitatively the effect of the gap on the imaging performance of the lens, snapshots of the magnetic field in the $x - z$ plane calculated using CST Microwave Studio are shown in Fig. 24 at $f = 19\,\text{THz}$ for different values of the gap size. It can be observed that for $g = 10\,\text{nm}$ [Fig. 24(a)], the results are promising and consistent with those for the ideal contact case (Fig. 12). The

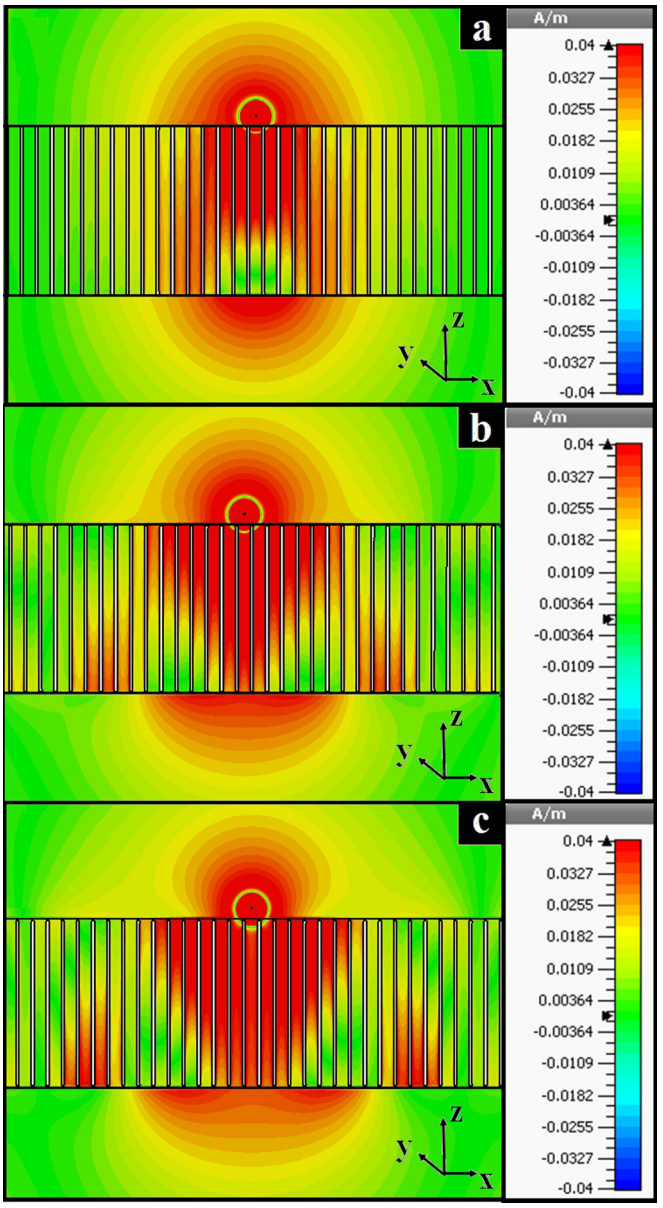

FIG. 24. (Color online) CST simulation results for the magnetic field distribution (H_y) of a WM slab loaded with graphene sheets for different values of the gap size: (a) $g = 10\,\text{nm}$, (b) $g = 15\,\text{nm}$, and (c) $g = 25\,\text{nm}$.

magnetic field distributions for $g = 15\,\text{nm}$ and $g = 25\,\text{nm}$, which are shown in Figs. 24(b) and 24(c), respectively, confirm the deterioration effect with the increase of the gap size.

It is worth mentioning that if the wires are embedded in a dielectric slab such as SiO_2, the fabrication of the lens becomes easier in a way that the gap allows the graphene to be attached to the substrate and avoids a direct connection of wires to graphene. This also relaxes the requirements on the wires, as it is only important that the wires do not protrude from the substrate. Our paper shows that for a WM slab loaded with graphene sheets with the following parameters of $a = 215\,\text{nm}$, $r_0 = 21.5\,\text{nm}$, $\mu_c = 1.5\,\text{eV}$, and $h = 2400\,\text{nm}$, by embedding the wires in a dielectric with the permittivity of $\varepsilon_h = 4$, the dispersion relation of the structure with the ideal contact shifts to lower frequencies, and subwavelength imaging can be obtained at the frequencies around $f = 9.8\,\text{THz}$ with the resolution of $\lambda/8.334$. According to our paper, it has been concluded that the required gap size to restore the fine details of the source at the image plane will be $g = 1\,\text{nm}$, which is smaller than that of the WM in the air due to the fast damping of the surface plasmons of the graphene in the dielectric spacer medium, which prevents the adequate surface plasmon coupling of the graphene sheets and the WM slab. The results are omitted here for the sake of brevity.

VII. CONCLUSIONS

In summary, a possibility of subwavelengh imaging by a WM slab loaded with graphene sheets is investigated. It has been shown that the presence of graphene provides significant flexibility in designing a subwavelength imaging device at THz frequencies. The physical mechanism behind the operation of our lens is based on the enhancement of evanescent waves. The presence of wires improves the strong coupling of the surface plasmons supported by the upper and lower interfaces of the structure. This lens not only has the advantages of operating in a wideband region, due to graphene's tunability and low loss sensitivity, but also has the possibility of increasing the structure's thickness. In addition, the source/image plane can be located at a distance larger than the lattice constant of the WM slab. The severe challenges in the implementation of the proposed lens have been investigated, and a promising approach in order to overcome those difficulties has been proposed. The results are studied analytically and validated against the full-wave numerical results obtained with CST Microwave Studio.

ACKNOWLEDGMENTS

The authors would like to acknowledge the helpful discussions with George W. Hanson, Gabriel Moreno, Mario G. Silveirinha, and Stanislav I. Maslovski. The authors are also grateful to the reviewers for their valuable comments. This paper has been partially supported by the NASA Experimental Program to Stimulate Competitive Research (EPSCoR) Award No. NNX13AB31A.

[1] V. G. Veselago, Sov. Phys. Usp. **10**, 509 (1968).
[2] J. B. Pendry, Phys. Rev. Lett. **85**, 3966 (2000).
[3] S. A. Ramakrishna, J. B. Pendry, M. C. K. Wiltshire, and W. J. Stewart, J. Mod. Opt. **50**, 1419 (2003).
[4] A. Grbic and G. V. Eleftheriades, Phys. Rev. Lett. **92**, 117403 (2004).
[5] T. Taubner, D. Korobkin, Y. Urzhumov, G. Shvets, and R. Hillenbrand, Science **313**, 1595 (2006).
[6] R. Merlin, Science **317**, 927 (2007).
[7] S. C. Kehr, Y. M. Liu, L. W. Martin, P. Yu, M. Gajek, S. Y. Yang, C.-H. Yang, M. T. Wenzel, R. Jacob, H.-G. von Ribbeck, M. Helm, X. Zhang, L. M. Esh, and R. Ramesh, Opt. Mater. Express **1**, 1051 (2011).
[8] P. Li and T. Taubner, Opt. Express **20**, 11787 (2012).
[9] H. Liu, B. Wang, L. Ke, J. Deng, C. C. Chum, S. L. Teo, L. Shen, S. A. Maier, and J. H. Teng, Nano Lett. **12**, 1549 (2012).
[10] S. Maslovski, S. Tretyakov, and P. Alitalo, J. Appl. Phys. **96**, 1293 (2004).
[11] S. I. Maslovski and S. A. Tretyakov, J. Appl. Phys. **94**, 4241 (2003).
[12] S. I. Maslovski, Opt. Commun. **285**, 3363 (2012).
[13] S. I. Maslovski and S. A. Tretyakov, New J. Phys. **14**, 035007 (2012).
[14] G. W. Hanson, J. Appl. Phys. **104**, 084314 (2008).
[15] B. Wang, Z. Xiang, Y. Xiaocong, and T. Jinghua, Appl. Phys. Lett. **100**, 131111 (2012).
[16] G. W. Hanson, J. Appl. Phys. **103**, 064302 (2008).
[17] A. Vakil, and N. Engheta, Science **332**, 1291 (2011).
[18] G. W. Hanson, A. B. Yakovlev, and A. Mafi, J. Appl. Phys. **110**, 114305 (2011).
[19] A. Andryieuski, A. V. Lavrinenko, and D. N. Chigrin, Phys. Rev. B **86**, 121108 (2012).
[20] T. Zhang, L. Chen, and X. Li, Opt. Express **21**, 20888 (2013).
[21] P. Li and T. Taubner, ACS Nano **6**, 10107 (2012).
[22] P. Ikonen, P. Belov, C. Simovski, and S. Maslovski, Phys. Rev. B **73**, 073102 (2006).
[23] P. A. Belov and M. G. Silveirinha, Phys. Rev. E **73**, 056607 (2006).
[24] M. G. Silveirinha, P. A. Belov, and C. R. Simovski, Phys. Rev. B **75**, 035108 (2007).
[25] M. G. Silveirinha, P. A. Belov, and C. R. Simovski, Opt. Let. **33**, 1726 (2008).
[26] C. S. R. Kaipa, A. B. Yakovlev, G. W. Hanson, Y. R. Padooru, F. Medina, and F. Mesa, Phys. Rev. B **85**, 245407 (2012).
[27] C. S. R. Kaipa, A. B.Yakovlev, F. Medina, F. Mesa, C. A. M. Butler, and A. P. Hibbins, Opt. Express **18**, 13309 (2010).
[28] Y. Fan, Z. Wei, H. Li, H. Chen, and C. M. Soukoulis, Phys. Rev. B **88**, 241403 (2013).
[29] A. B. Yakovlev, Y. R. Padooru, G. W. Hanson, A. Mafi, and S. Karbasi, IEEE Trans. Microwave Theory Tech. **59**, 527 (2011).
[30] A. B. Yakovlev, Y. R. Padooru, S. Karbasi, G. W. Hanson, and A. Mafi, in *IEEE AP-S International Symposium on Antennas and Propagation and CNC-USNC/URSI Radio Science*

Meeting, Toronto, Canada, July 11-17 (IEEE, New York, 2010), pp. 1–4.
[31] C. S. R. Kaipa, A. B. Yakovlev, S. I. Maslovski, and M. G. Silveirinha, Phys. Rev. B **86**, 155103 (2012).
[32] B. D. F. Casse, W. T. Lu, Y. J. Huang, E. Gultepe, L. Menon, and S. Sridhar, Appl. Phys. Lett. **96**, 023114 (2010).
[33] S. H. Jiang and R. Pike, New J. Phys. **7**, 169 (2005).
[34] P. Kolinko and D. Smith, Opt. Express **11**, 640 (2003).
[35] W. T. Lu and S. Sridhar, Microw. Opt. Tech. Lett. **39**, 282 (2003).
[36] X. Yang, Y. Liu, J. Ma, J. Cui, H. Xing, W. Wang, C. Wang, and X. Luo, Opt. Express **16**, 19686 (2008).
[37] CST Microwave Studio 2014, CST GmbH http://www.cst.com.
[38] P. A. Belov, Y. Zhao, S. Sudhakaran, A. Alomainy, and Y. Hao, Appl. Phys. Lett. **89**, 262109 (2006).
[39] Z. Wei, Y. Cao, Z. Gong, X. Su, Y. Fan, C. Wu, J. Zhang, and H. Li, Phys. Rev. B **88**, 195123 (2013).
[40] A. Reina, X. Jia, J. Ho, D. Nezich, H. Son, V. Bulovic, M. S. Dresselhaus, and J. Kong, Nano Lett. **9**, 30 (2008).
[41] P. W. Sutter, J-I Flege, and E. A. Sutter, Nat. Mater. **7**, 406 (2008).
[42] A. Reina, H. Son, L. Jiao, B. Fan, M. S. Dresselhaus, Z. Liu, and J. Kong, J. of Phys. Chem. C **112**, 17741 (2008).
[43] M. G. Silveirinha, IEEE Trans. Antennas Propag. **54**, 1766 (2006).
[44] M. G. Silveirinha, C. A. Fernandes, and J. R. Costa, New J. Phys. **10**, 053011 (2008).
[45] O. Luukkonen, M. G. Silveirinha, A. B. Yakovlev, C. R. Simovski, I. S. Nefedov, and S. A. Tretyakov, IEEE Trans. Microwave Theory Tech. **57**, 2692 (2009).
[46] A. B. Yakovlev, M. G. Silveirinha, O. Luukkonen, C. R. Simovski, I. S. Nefedov, and S. A. Tretyakov, IEEE Trans. Microwave Theory Tech. **57**, 2700 (2009).
[47] M. G. Silveirinha, C. A. Fernandes, and J. R. Costa, IEEE Trans. Antennas Propag. **56**, 405 (2008).
[48] M. G. Silveirinha, and C. A. Fernandes, IEEE Trans. Microwave Theory Tech. **53**, 1418 (2005).
[49] L. Solymar, and E. Shamonina, *Waves in Metamaterials* (Oxford University Press, New York, 2009)
[50] F. Medina, F. Mesa, and D. C. Skigin, IEEE Trans. Microwave Theory Tech. **58**, 105 (2010).
[51] C. S. Kaipa, A. B. Yakovlev, F. Medina, and F. Mesa, J. Appl. Phys. **112**, 033101 (2012).
[52] Y. Zhao, P. A. Belov, and Y. Hao, Opt. express **14**, 5154 (2006).
[53] M. Born and E. Wolf, *Principles of Optics* (Cambridge University Press, Cambridge, 1999).
[54] X. Li, F. Gao, and Z. Gu, Open Surf. Sci. J. **3**, 91 (2011).